Ultrasonics Sonochemistry 80 (2021) 105829

Contents lists available at ScienceDirect

Ultrasonics Sonochemistry

journal homepage: www.elsevier.com/locate/ultson

The growth restriction effect of TiCN nanoparticles on Al-Cu-Zr alloys via ultrasonic treatment

Yiwang Jia [a,*], Dongfu Song [a,b], Nan Zhou [a], Kaihong Zheng [a], Yanan Fu [c], Da Shu [d]

[a] Guangdong Provincial Key Laboratory of Metal Toughening Technology and Application, Institute of New Materials, Guangdong Academy of Sciences, Guangzhou 510650, China
[b] National Engineering Research Center of Near-net-shape Forming for Metallic Materials, South China University of Technology, Guangzhou 510641, China
[c] Shanghai Synchrotron Radiation Facility, Shanghai Institute of Applied Physics, CAS, Shanghai 201204, China
[d] Shanghai Key Lab of Advanced High-temperature Materials and Precision Forming, School of Materials Science and Engineering, Shanghai Jiao Tong University, Shanghai 200240, China

ARTICLE INFO

Keywords:
X- radiography
$TiCN_{np}$
Ultrasonic treatment
Al-Zr alloy
Modeling

ABSTRACT

Ex situ and in situ synchrotron X-radiography study on Al-Cu-Zr alloys with addition of Al-5Ti-1B and TiCN nanoparticles ($TiCN_{np}$) were carried out at different cooling rates. Al-Zr alloy can be effectively refined by $TiCN_{np}$ via Ultrasonic treatment as compared with Al-5Ti-1B which has Zr poisoning effect. The influence of cooling rate on the nucleation and growth of grains have been studied quantitatively. The results show that the grain size was decreased and the growth rate was increased with the increasing of cooling rate. At the same cooling rate, the grain size with addition of 0.5% $TiCN_{np}$ was smaller than that with the same addition of Al-5Ti-1B. The blocking factor f of $TiCN_{np}$ decreases with increasing cooling rate. Based on the free growth model, a new numerical model considering the growth restriction effect of nanoparticles was established. The growth of grain was inhibited by the combining effect of solute and nanoparticles. The growth rate of grain is reduced due to part of the solid/liquid interface coated by nanoparticles. The blocking factor f is linearly decreased with the coverage ratio ω which is proportional to the critical grain radius. The grain size decreases with increasing cooling rate and decreasing f . This study is especially beneficial for Al alloys that have poisoning phenomenon inoculated by traditional refiner.

1. Introduction

High-strength aluminum alloys containing trace amounts of Zr element are widely used in the aerospace field [1]. The addition of Zr element can form a fine and dispersed Al_3Zr phase[2], which can reduce the quenching sensitivity of the Al alloy, inhibit recrystallization during heat treatment, increase the dislocation density, and improve the mechanical properties of the Al alloy[3]. The Zr-containing aluminum alloy can also effectively retain the small-angle grain boundaries obtained by processing deformation and improve the stress corrosion resistance of the Al alloy [4]. Therefore, adding a small amount of Zr element can comprehensively improve the strength, toughness and corrosion resistance of the Al alloy [5].

However, traditional grain refiners such as Al-Ti-B [6] or Al-Ti-C [7] have poisoning phenomenon when refining Zr-containing aluminum alloys [8]. At present, The Zr poisoning theory is divided into two categories. One is that Zr deteriorates the nucleation potency of the nucleation sites[6]. The other is that Zr depletes the alloying elements reducing the restriction effect of grain growth [9,10]. The Synchrotron radiation X-radiography research [11] found that the degree of nucleation undercooling and the grain growth velocity increased with addition of Zr. Zr poisoning is caused by the simultaneous increase in solute suppressed nucleation zone and the average interparticle spacing of the most potent TiB_2 particles. Thus it is necessary to find a new refinement method for Zr-containing Al alloy.

Recent studies have shown that commercial purity aluminum (CPAl) [12], Al-Cu [13] and Al-Si alloys[14–16] can be effectively refined by a small amount of TiCN nanoparticles ($TiCN_{np}$) which were dispersed into the matrix by high-energy ultrasound treatment. Chen *et al.* [17] added $TiC_{0.7}N_{0.3}$ nanoparticles with a volume fraction of 2% to the Al-20Bi alloy which were dispersed in the matrix after ultrasonic treatment. As a result, the size of the Bi phase was reduced from 821 μm to ~ 7.5 μm. Levi *et al.* [18] found that $TiCN_{np}$ can refine the Mg_2Si phase in Al-Mg-Si

* Corresponding author.
E-mail address: ywjia@gimp.gd.cn (Y. Jia).

https://doi.org/10.1016/j.ultsonch.2021.105829
Received 19 September 2021; Received in revised form 4 November 2021; Accepted 11 November 2021
Available online 12 November 2021

Nomenclature

f	the blocking factor
ΔT_{fg}	the free growth undercooling (K)
σ	the solid–liquid interfacial energy (J/m^2)
ΔS_v	the entropy of fusion per unit volume (J/(K·m^3))
d	the nanoparticle diameter (nm)
Q	the growth restriction factor (K)
m	the liquidus slope (K/wt.%)
k	the equilibrium partition coefficient
C_0	the solute concentration (wt.%)
r	the radius of spherical grain (μm)
ΔT	the total undercooling (K)
ΔT_c	the curvature undercooling (K)
t	time (s)
D_s	the solute diffusion coefficient (m^2/s)
λ_s	obtained by S
S	a constant related to the undercooling
V	the growth rate of spherical grains (μm/s)
dr	the radius of spherical grain interval (μm)
dt	the time interval (s)
R	the cooling rate of the melt (K/s)
T_n	the melt temperature at nth time interval (K)
N	the total number of grains
$N(d)$	the size distribution function of $TiCN_{np}$
N_n	$TiCN_{np}$ participating in nucleation in the nth time interval
$q_{(i,n)}$	the latent heat released in the ith time interval (J)
ΔH_V	the latent heat of solidification per unit volume (J/m^3)
Q_n	the whole latent heat (J)
C_{pV}	the specific heat of the melt per unit volume (J/mm^3)
N_0	the total number of $TiCN_{np}$
d_0	the geometric mean of the distribution (μm)
Δd	the particle diameter interval (μm)
V	the volume of FOV (μm^3)
v_{np}	the growth rate with addition of $TiCN_{np}$ (μm/s)
v_{gr}	the growth rate with addition of Al-5Ti-1B (μm/s)
ω	the coverage ratio of $TiCN_{np}$
a, b	constant
P_v	the volume percent of $TiCN_{np}$
r_g	the radius of growing grain (μm)

alloys and proposed an irreversible adsorption model. Adding 2% volume fraction of $TiCN_{np}$ can refine the grain size of CPAl to 138 μm [19], and the hardness, strength and plasticity of the material have been greatly improved.[20]

The effects of $TiCN_{np}$ added to Al melts have opened a new field of grain refinement.[21] On the one hand, $TiCN_{np}$ is a potency nucleation site for α-Al which has an orientation relationship of $(\bar{1}\bar{1}1)_{Al}[0\,1\,1]_{Al}//(\bar{1}\bar{1}1)_{NP}[0\,1\,1]_{NP}$ analyzed by high resolution transmission electron microscopy.[12] On the other hand, nanoparticles are attached to the surface of the crystal grains in a very short time [17], which hinders the migration of solute elements at the interface. As the crystal grows, the nanoparticles are moved and accumulated on the solid/liquid (S/L) interface, reducing the growth of crystal grains. This allows the melt to form a large degree of undercooling, thereby inducing more nucleation behavior.

However, the hypothesis that $TiCN_{np}$ wraps on the surface of crystal grains to inhibit growth is only an post-mortem research. There is a lack of real-time solidification process research, and the accuracy of the theoretical model needs to be further verified. The in situ synchrotron radiation observation of the solidification of metals has a history of more than 20 years [22–24]. With the increase of the energy of the light source and the advancement of the equipment, it has better spatial and temporal resolution. At the same time, image processing methods for imaging experimental data are also advancing with the times[25], which can quantitatively calculate nucleation rate[26,27], nucleation undercooling[28], solute concentration[29], solid phase thickness[30] and nanoparticles on dendritic grain growth[31,32]. Al-Cu alloys added with TiC nanoparticles were investigated by in situ X-radiography[33] which found that the TiC nanoparticles promoted heterogeneous nucleation of α-Al. The machine learning algorithm is applied to the processing of experimental data, which can fully track the nucleation and growth process of all crystal grains[34].

As Al alloy containing Zr cannot be refined by traditional grain refiner, the aim is to find a new refinement method by nanoparticles and reveal the mechanism. In the current study, ex situ and in situ synchrotron X-radiography technique were adopted to research the growth restriction effect of $TiCN_{np}$ on Al-Zr alloys. The influence of cooling rate on the nucleation and growth of grains of Al-Cu-Zr alloys with addition of Al-Ti-B and $TiCN_{np}$ have been quantitatively studied. With the blocking factor f obtained from the in situ experiments, a new numerical model considering the growth restriction effect of nanoparticle has been established based on free growth model.

2. Experimental procedure

2.1. Raw materials

The raw materials are CPAl (99.6%, all compositions are in weight percent unless specified.), high purity Cu (99.9%), Al-10Zr (99.5%) master alloy and $TiC_{0.5}N_{0.5}$ nanoparticles (99%). The size distribution of $TiCN_{np}$ was determined from image analysis of scanning electron micrographs. More than 4000 $TiCN_{np}$ were measured for obtaining the size distribution[35]. It was well fitted by a lognormal function as shown in Fig. 1(a).

$$N(d) = \frac{N_0 \bullet \Delta d}{\sigma d\sqrt{2\pi}}\, exp\left(-\frac{(ln(d) - ln(d_0))^2}{2\sigma^2}\right) \quad [1]$$

Where $N(d)$ is the number of nanoparticles with a diameter between d and $d+\Delta d$. N_0 is the total number of $TiCN_{np}$, d_0 is the geometric mean value of the distribution, which is 78.2 nm, and σ is the geometric standard deviation, which is 0.444.

2.2. Grain refinement tests

Grain refinement experiments were carried out on Al-0.2Zr alloy with addition of 0.2% Al-Ti-B master alloy(99.5%) and 0.5% $TiCN_{np}$ using the Reynolds standard golf T-mold method[35]. CPAl and Al-Zr alloy which placed in an alumina crucible melted in a resistance furnace, while Ar gas is introduced into the crucible to reduce oxidation. After holding at 750 °C for 10 min, $TiCN_{np}$ which was preheated at 300 °C for 2 h and wrapped in Al foil was added into the melt. The ultrasonic treatment promotes the dispersion of $TiCN_{np}$ as shown in Fig. 1 (c). The ultrasonic frequency is 20KHz, power is 1500 W, and the time is 5 min. The melt was cast into a Reynolds standard golf T-mold after ultrasonic treatment.

After the sample was polished and corroded by Keller reagent, the metallographic structure was observed with an optical microscope, and the grain size was measured by the linear intercept method. The field emission scanning electron microscope (SEM) with energy dispersive spectrometry (EDS) was used to observe the microstructure of the

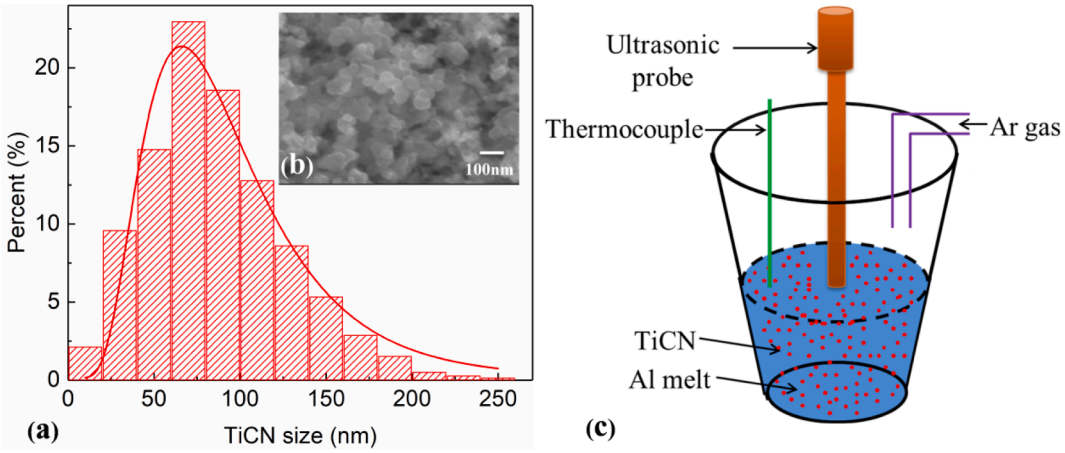

Fig. 1. (a) Size distribution of $TiCN_{np}$; (b)SEM microstructure of $TiCN_{np}$; (c) The illustration of ultrasonic treatment.

sample and the size distribution of $TiCN_{np}$. The composition was analyzed by inductively coupled emission spectrometer (ICP).

2.3. In situ X-radiography experiments

Al-Cu alloy system has smaller distribution coefficient and larger atomic number difference between Al and Cu element, thus it has good solid–liquid imaging contrast. In order to minimize the effects of convection and grains motion, we chose Al-13%Cu-0.2%Zr alloy as the base alloy, which has a slightly difference in the densities of solid phase and bulk melt. Al-13Cu-0.2Zr alloys with addition of 0.5% Al-5Ti-1B and 0.5% $TiCN_{np}$ were prepared by ultrasonic treatment as mentioned in part 2.2. The as-cast ingots were cut into thin slices of 15 mm × 10 mm×~0.22 mm with the surface polished. The details were in our previous reports [11,28,30,36,37].

The in situ synchrotron X-radiography experiments were carried out on beamline BL13W1[38] at the Shanghai Synchrotron Radiation Facility (SSRF). Detailed X-radiography parameters are listed in Table 1. The incident monochromatic X-ray energy was calibrated as 18 keV, and the distance between the sample and the CCD was 20 cm to obtain the best absorption contrast for the chosen alloy system. The images were recorded by the CCD camera at a rate of 1 frame/s. A spatial field-of-view (FOV) of 4225 μm × 4225 μm with a pixel size of 3.25 μm was obtained after image processing. The volume of the FOV is calculated by multiplying the thickness and area of each sample. The sample was cooling down at different rates (0.2, 0.3, 0.5, 1 and 1.5 K/s). The furnace was operated in the near-isothermal mode with the two heaters cooling at the same rate simultaneously.

3. Experimental results

3.1. Grain refinement results

Fig. 2 shows the macrographs sectioned at 51 cm above the base of Al-0.2Zr alloy under Reynolds standard golf Tee mold condition. The grain size of CPAl refined by 0.1% Al-5Ti-1B is about 175 μm as reported by Wang et al[6]. However, the grain obviously becomes coarse after adding 0.2% Zr to the CPAl due to Zr poisoning effect as shown in Fig. 2 (a). Fig. 2(b) shows a fine and fully equiaxed grain structure of Al-0.2Zr alloy refined by 0.5% $TiCN_{np}$. The optical microstructures are shown in Fig. 2(c) and 2(d). More than 10 microstructure pictures are measured by equivalent area diameter method to obtain the average grain size of each sample. The average grain size of Al-0.2Zr alloy is 682 μm with addition of 0.5% Al-5Ti-1B and 97 μm with addition of 0.5% $TiCN_{np}$. This suggests that $TiCN_{np}$ can effectively overcome the effect of Zr poisoning.

Table 1
The setup of X-radiography experiment.

Energy (keV)	Pixel size (μm)	Temporal resolution (Hz)	FOV (mm^2)
18	3.25	1	4.225 × 4.225

The SEM results of Al-0.2Zr alloy with addition of 0.5% $TiCN_{np}$ show in Fig. 3. It can be confirmed from the EDS result of spectrum 1 that the particles inside the grain are $TiCN_{np}$. The Ti mapping indicates the distribution of $TiCN_{np}$, given that the EDS detector fail to detect the light elements such as C and N[15]. As shown in Fig. 3(a), a small number of $TiCN_{np}$ was dispersed intra-granular and a majority of $TiCN_{np}$ was agglomerated along the grain boundaries. The width of the $TiCN_{np}$ on the grain boundaries was several hundred nanometers.

3.2. X-radiography results

Fig. 4 shows the image sequences of in situ X-radiography experiments of Al-13Cu-0.2Zr alloys with addition of 0.5% Al-Ti-B at different cooling rates (0.2, 0.3, 0.5, 1 and 1.5 K/s). The origin time set to be the first appearance of the grain. Supplementary videos of the experiments at the cooling rate of 0.2 K/s are available on line. After image processing, the grains with a low solute concentration appear in blue, because of the low absorption of X-ray. With the growth up of the grains, more solute is expelled into the liquid phase. Thus the liquid phase with a high solute concentration appears in red. As the cooling rate increases, more grains appear in the FOV. The grains number in the FOV is 174, 301, 396, 492 and 683 at cooling rates of 0.2, 0.3, 0.5, 1 and 1.5 K/s respectively. Thus the grain size can be calculated from Eq. [2], which is 339, 282, 258, 240 and 218 μm respectively.

$$d = \left(\frac{6V}{\pi N}\right)^{1/3} \quad [2]$$

Where V is the volume of the FOV, and N is the total grains in the FOV.

Fig. 5 shows the image sequences of Al-13Cu-0.2Zr alloys with addition of 0.5% $TiCN_{np}$ at different cooling rates (0.2, 0.3, 0.5, 1 and 1.5 K/s). The number of grains also increases with the increasing of cooling rate. At the same cooling rate, the grain size was obviously smaller than that of Al-5Ti-1B. The grains number in the FOV is 401, 535, 761, 1082 and 1511 at cooling rates of 0.2, 0.3, 0.5, 1 and 1.5 K/s respectively. Thus the grain size is 256, 233, 207, 184 and 142 μm calculated from Eq. [2] respectively.

In order to investigate the effect of $TiCN_{np}$ on the growth of grains, two grains were chosen from each X-radiography experiments for analysis. The criteria for selection were that the grain was stationary in favor of statistics and initially isolated from the surrounding grains. In

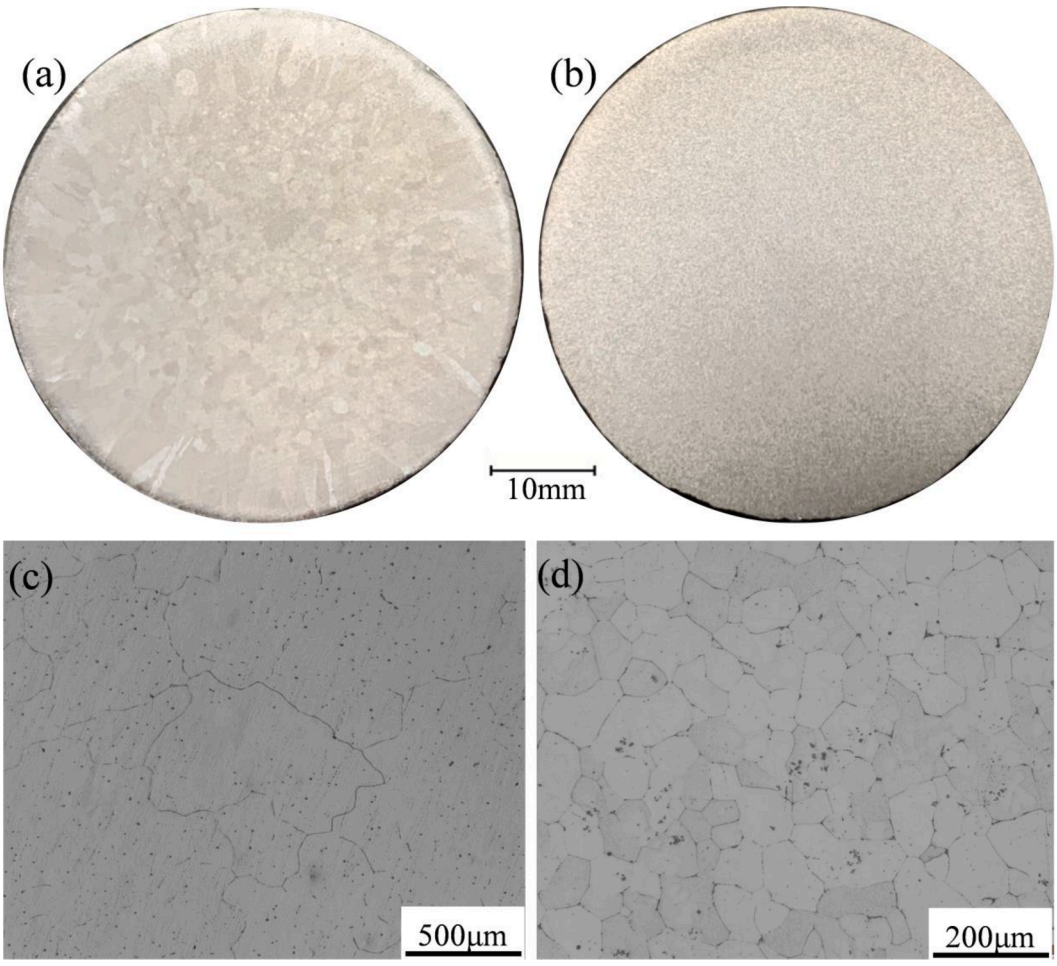

Fig. 2. Macrographs and optical microstructures of Al-0.2Zr alloy solidified in the T-mold. (a)&(c) Addition of 0.5% Al-5Ti-1B; (b)&(d) Addition of 0.5% $TiCN_{np}$.

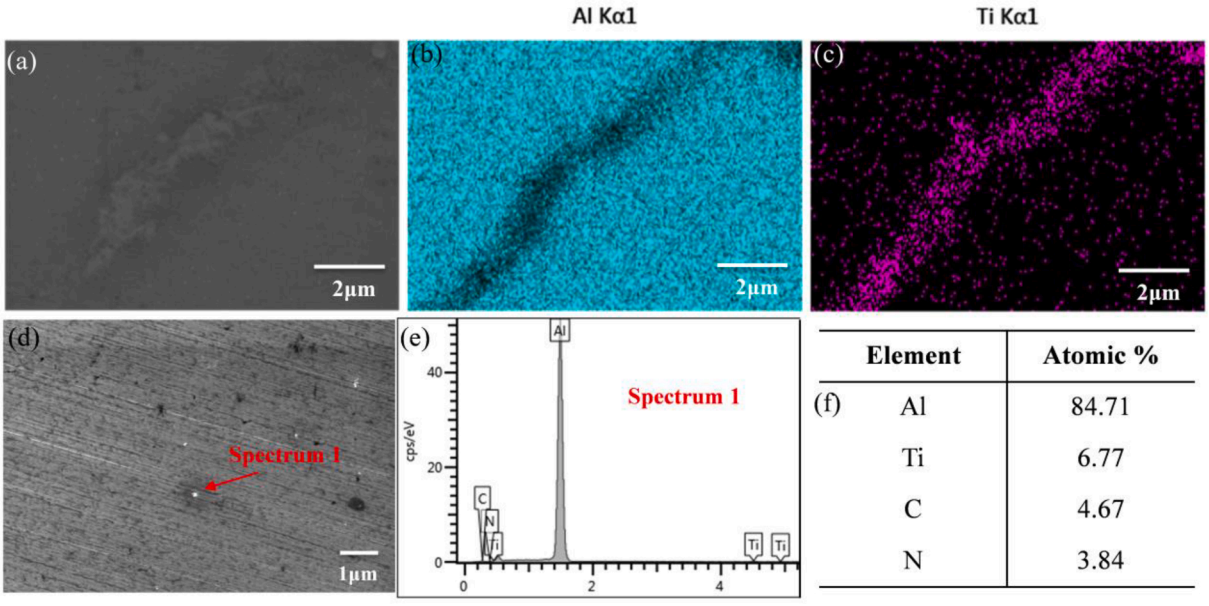

	Element	Atomic %
(f)	Al	84.71
	Ti	6.77
	C	4.67
	N	3.84

Fig. 3. (a)&(d) SEM micrographs of Al-0.2Zr refined by 0.5% $TiCN_{np}$; (b) Al mapping; (c) Ti mapping; (e) Spectrum 1; (f) Atomic percent of spectrum 1.

addition, the influence of gravity can be ignored. The grain growth is nearly spherical as shown in Fig. 4 and Fig. 5. Thus the grain growth rate can be calculated by the variation in the radius with time. The time evolution of radii with addition of Al-5Ti-1B and $TiCN_{np}$ at different cooling rates is shown in Fig. 6. Due to the spatial resolution limitation, the grains had grown to about 20 μm in diameter by the time they

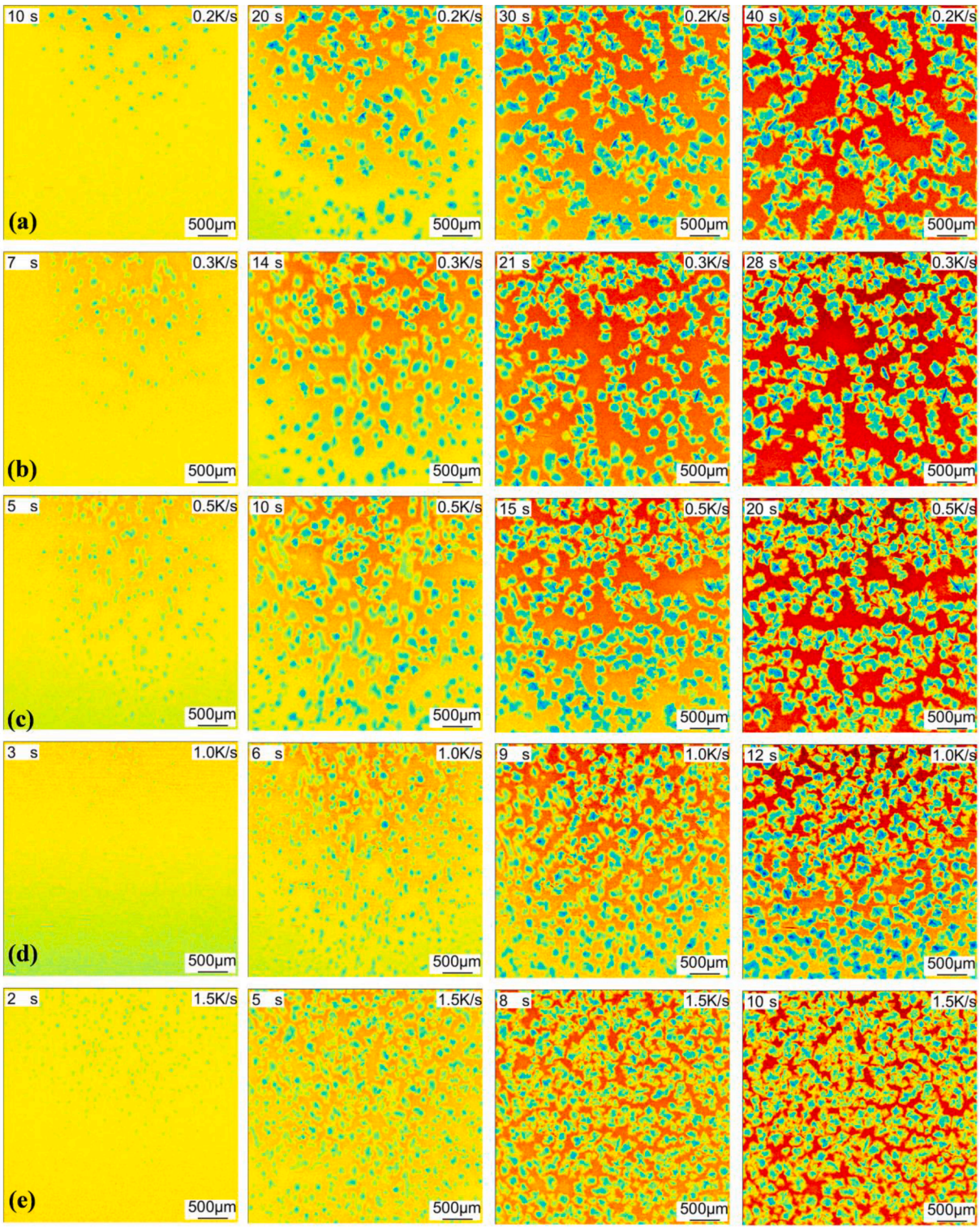

Fig. 4. Image sequences of Al-13Cu-0.2Zr alloys with addition of 0.5% Al-5Ti-1B at different cooling rates. (a) 0.2 K/s; (b) 0.3 K/s; (c) 0.5 K/s; (d) 1 K/s; (e) 1.5 K/s.

became measurable and the error was about ± 10 μm.

The main purpose of this paper is to study the blocking effect of nanoparticle. At the same cooling rate, the rate of heat released to the outside is the same. As the DSC curve shown in Fig. 7, the temperature at the beginning of the solidification of Al-13Cu-0.2Zr alloy with addition of Al-5Ti-1B and $TiCN_{np}$ is 622.89℃ and 623.02℃ respectively. The difference is only 0.13℃. Thus we assume the driving force for the grain growth is the same with addition of Al-5Ti-1B and $TiCN_{np}$. As the free Ti in the melt is only 0.014 wt% with addition of 0.5% Al-5Ti-1B. Comparing with the Q of Cu which is 38 K, the Q of Ti is less than 1 K. So we assume the growth restriction effect by the solute is the same with addition of Al-5Ti-1B and $TiCN_{np}$. With addition of 0.5 wt% Al-5Ti-1B, the volume percent of TiB_2 in the melt is less than 0.01%. As a comparison, the volume percent of $TiCN_{np}$ is 0.164%. Thus the blocking of S/L interface growth by TiB_2 can be ignored. The main difference is the presence of nanoparticles ahead the S/L interface with addition of $TiCN_{np}$.

So the blocking factor f by $TiCN_{np}$ can be defined by the growth rate

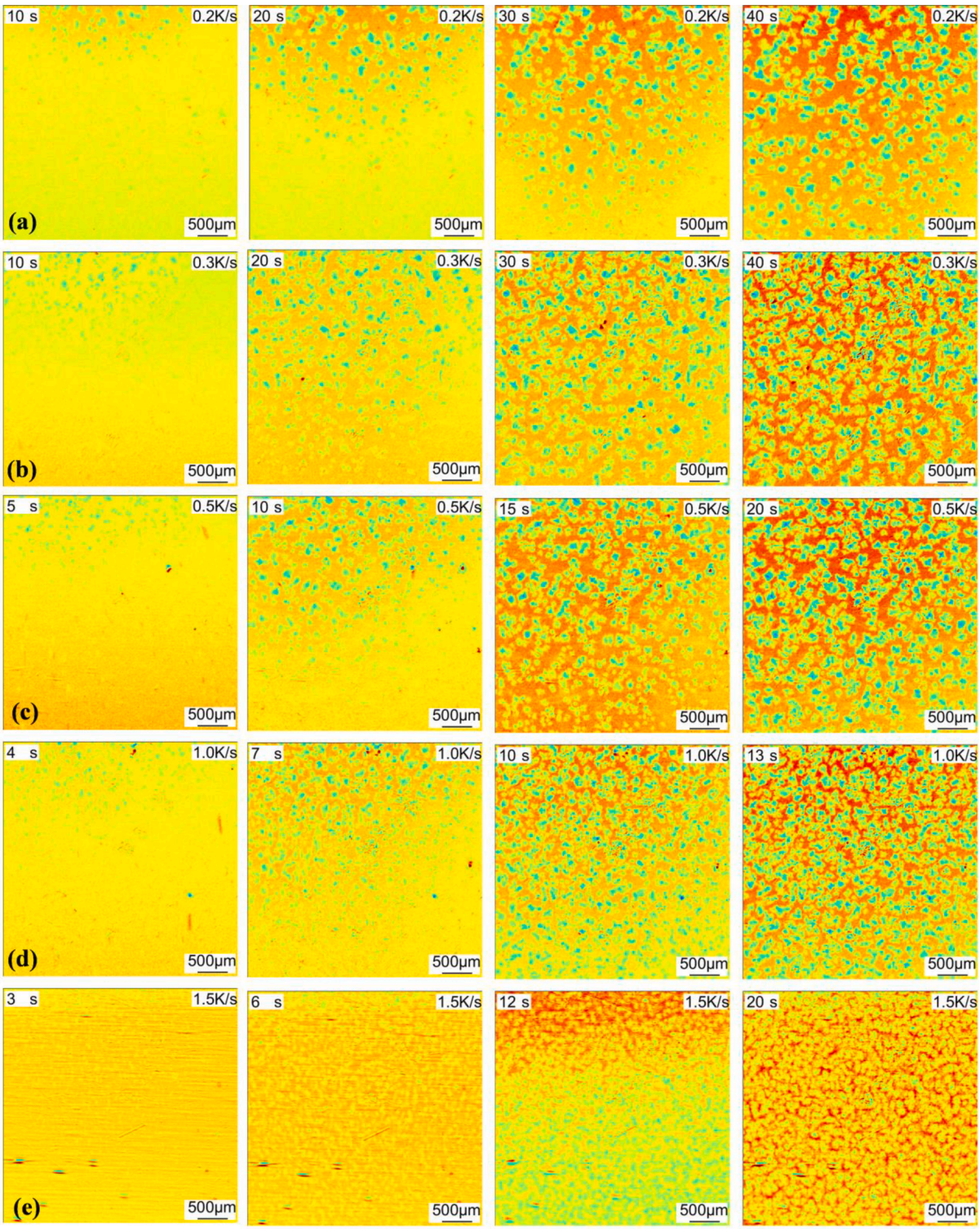

Fig. 5. Image sequences of Al-13Cu-0.2Zr alloys with addition of 0.5% $TiCN_{np}$ at different cooling rates. (a) 0.2 K/s; (b) 0.3 K/s; (c) 0.5 K/s; (d) 1 K/s; (e) 1.5 K/s.

v_{np} with addition of $TiCN_{np}$ dividing the growth rate v_{gr} with addition of Al-5Ti-1B, *i.e*, $f = v_{np}/v_{gr}$. As shown in Table 2, the average growth rates of radius at cooling rates of 0.2, 0.3, 0.5, 1, 1.5 K/s are 8.3, 11.03, 13.78, 15.44, 17.41 μm/s with addition of Al-Ti-B and 4.55, 6.79, 9.05, 11.07, 13.2 μm/s with addition of $TiCN_{np}$ respectively (Table 2). Thus, f is 0.547, 0.615, 0.657, 0.717 and 0.758 at cooling rates of 0.2, 0.3, 0.5, 1 and 1.5 K/s respectively. This indicates that the blocking factor of $TiCN_{np}$ decreases with increasing of cooling rate.

4. Modeling of growth restriction effect of nanoparticle

Wang *et al.* [12] studied the Al/$TiCN_{np}$ interface using HRTEM. There had good lattice matching between Al matrix and $TiCN_{np}$. The orientation relationship is $(\overline{1}\,\overline{1}1)_{Al}[0\,1\,1]_{Al}//(\overline{1}\,\overline{1}1)_{NP}[0\,1\,1]_{NP}$ with a lattice misfit of 5.5%. If the misfit is less than 10%, an orientation relationship exists according to the edge to edge model [39]. This indicates that $TiCN_{np}$ is high potency nucleation sites for Al. The adsorption model

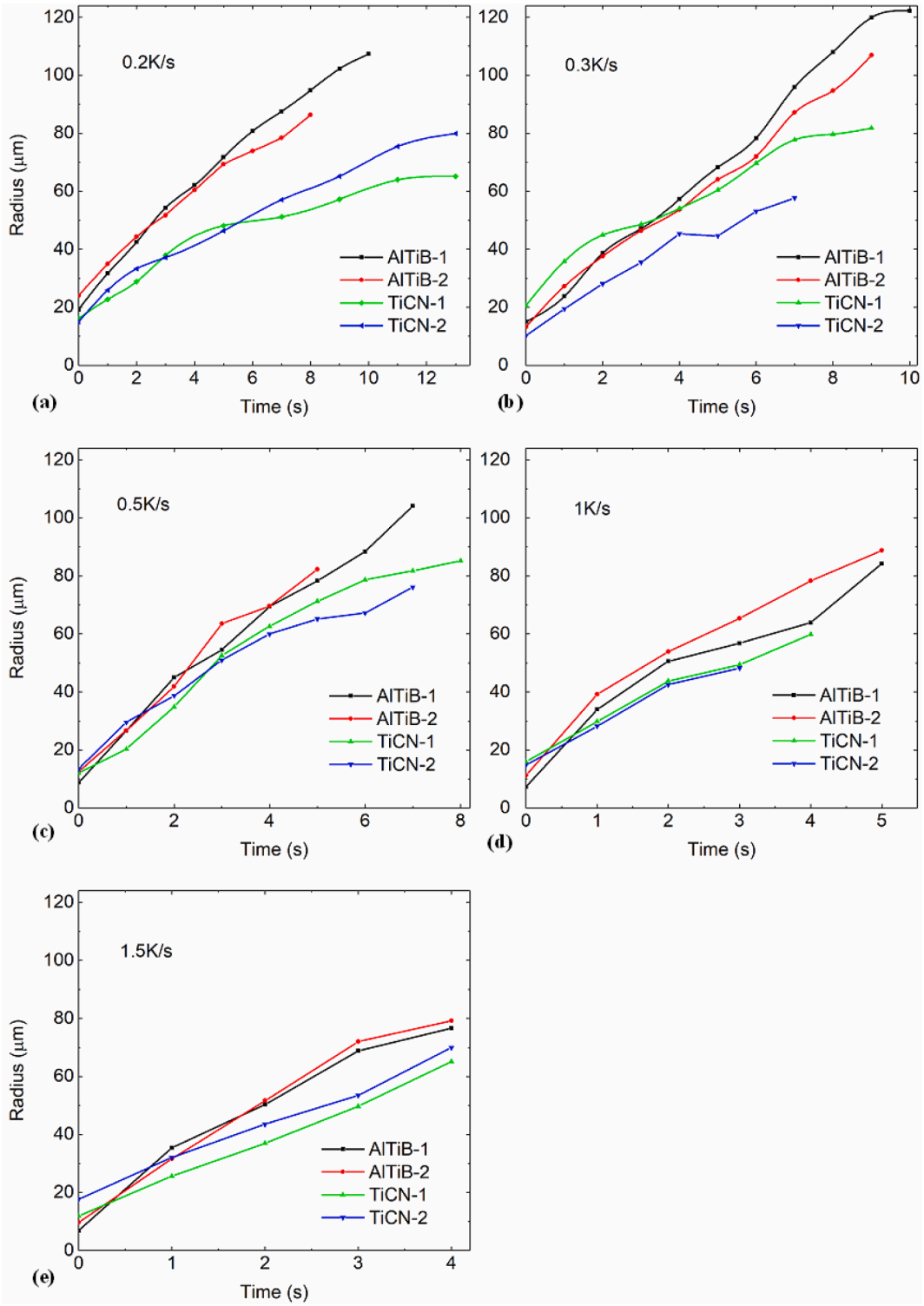

Fig. 6. Time evolution of the radius of grains at different cooling rates.

may be appropriate with such potent nucleation[40]. So we assume that the free growth condition determines the nucleation of Al on $TiCN_{np}$[41]. The nucleation undercooling ΔT_{fg} on a TiCN nanoparticle with diameter d is:

$$\Delta T_{fg} = \frac{4\sigma}{\Delta S_V d} \quad [3]$$

Where $\sigma = 158\times 10^{-3}$ J/m^2 is the S/L interfacial energy, and $\Delta S_v = 1.112 \times 10^6$ J/(Km^3) [41] is the entropy of fusion per unit volume. We assume that the melt is spatially isothermal for this small amount of alloy.

Growth restriction factor Q by the solute is defined by:

$$Q = mC_0(k-1) \quad [4]$$

Where m is the liquidus slope, k is the equilibrium partition coefficient, C_0 is the solute concentration.[42] Those parameters of Cu are listed in Table 3, so the Q is 38 K in this study. The influence of Zr to Q is neglected. The free Ti in the melt is only 0.014 wt% with addition of

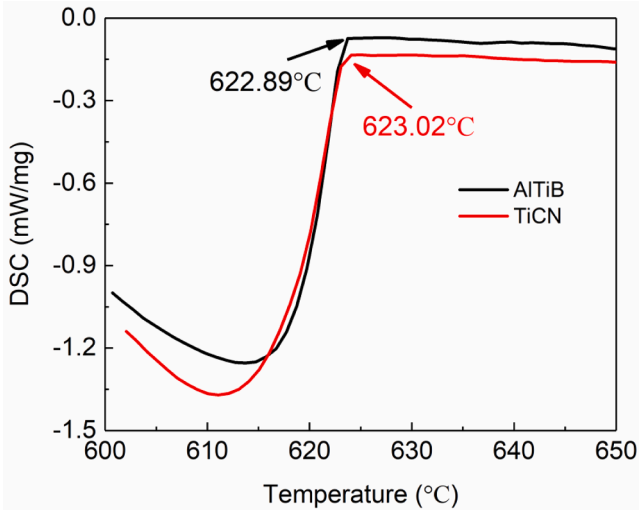

Fig. 7. DSC results of Al-13Cu-0.2Zr alloys with addition of Al-Ti-B and $TiCN_{np}$.

Table 2
The average growth rates of grains and blocking factor f at different cooling rates

Cooling rate (K/s)	0.2	0.3	0.5	1.0	1.5
v_{np} (μm/s)	4.55	6.79	9.05	11.07	13.2
v_{gr} (μm/s)	8.3	11.03	13.78	15.44	17.41
f	0.547	0.615	0.657	0.717	0.758

Table 3
The parameters of Cu used in the calculation

Element	m (K wt.%$^{-1}$)[43]	k [43]	C_0 (wt.%)	Q (K)
Cu	−3.4	0.14	13	38

0.5% Al-5Ti-1B. Thus the growth restriction factor Q and the influence to solute diffusion coefficient D_s by Ti can be neglected.

The grains shape can be taken to be spherical at early stage of solidification as shown in Figs. 4 and 5. When a spherical crystal[44] grows to a radius r, the curvature undercooling ΔT_c is:

$$\Delta T_c = \frac{2\sigma}{\Delta S_V \times r} \quad [5]$$

The spherical radius r has the following relationship with the time t in isothermal melt [45,46]:

$$r = \lambda_s (D_s t)^{1/2} \quad [6]$$

Where $D_s = 4.65 \times 10^{-9} m^2/s$ is the solute diffusion coefficient of Cu in the Aluminum melt [41]. λ_s can be obtained by:

$$\lambda_s = \left(\frac{-S}{2\pi^{\frac{1}{2}}}\right) + \left(\frac{S^2}{4\pi} - S\right)^{\frac{1}{2}} \quad [7]$$

S is given by[47]:

$$S = \frac{2\Delta T_c}{(k-1)\Delta T_c + Q} \quad [8]$$

The growth rate v_{gr} of a spherical grain can be obtained by differentiating Eq. [6] with respect to time:

$$v_{gr} = \frac{dr}{dt} = \frac{\lambda_s^2 D_s}{2r} \quad [9]$$

In the conventional grain refinement, the growth restriction is only by solute. However, the growth of grain is also restricted by the nanoparticles after the addition of $TiCN_{np}$. As there have nanoparticles in the melt, the interface migration could be pinned by $TiCN_{np}$. So we should consider the blocking factor f by $TiCN_{np}$. The blocking factor f defined by:

$$f = v_{np}/v_{gr} \quad [10]$$

Where v_{np} is the growth rate of grain with addition of $TiCN_{np}$ and v_{gr} is that without $TiCN_{np}$. f at different cooling rates had been obtained from in situ X-radiography experiments as shown in Table 2.

Thus the growth rate v_{np} with addition of $TiCN_{np}$ can be obtained by:

$$v_{np} = f \bullet v_{gr} = f \bullet \frac{\lambda_s^2 D_s}{2r} \quad [11]$$

The numerical calculation is performed by dividing time into a series of steps. The cooling rate is R, the time step duration dt is set to be 0.001 s. Before the beginning of solidification:

$$T_{n+1} = T_n - R^* dt \quad [12]$$

As the temperature decreases, nucleation begins on the largest nanoparticle. The size distribution of $TiCN_{np}$ is lognormal function $N(d)$ as shown in Fig. 1(a). In time increment dt, the diameter of $TiCN_{np}$ participating in nucleation decreases from d_n to d_{n+1}. The number N_n of nanoparticles participating in nucleation in the nth time interval is:

$$N_n = N(d)^*(d_n - d_{n+1}) \quad [13]$$

When one grain which is nucleated in the ith time interval grows to the nth time interval, the radius $r_{(i,n)}$ is obtained by:

$$r_{(i,n)} = r_{(i,n-1)} + v_{np,(i,n-1)}^* dt (1 \le i \le n) \quad [14]$$

In the nth time increment, the latent heat $q_{(i,n)}$ which is released by the grains nucleated in the ith increment is:

$$q_{(i,n)} = N_i^* 4\pi r_{(i,n-1)}^2 \left[r_{(i,n)} - r_{(i,n-1)}\right] \Delta H_V (1 \le i \le n) \quad [15]$$

where $\Delta H_V = 9.5 \times 10^8 J/m^3$ is the latent heat of solidification per unit volume. [41]

The whole latent heat Q_n which is released in the nth time increment is:

$$Q_n = \sum_{i=1}^{n} q_{(i,n)} \quad [16]$$

The melt temperature in the next time increment is then given by:

$$T_{n+1} = T_n - R^* dt + \frac{Q_n}{C_{pV}} \quad [17]$$

where $C_{pV} = 2.58 \times 10^6 J/(Km^3)$ is the specific heat of the melt per unit volume.[41]

When the latent heat released equals to the external heat extraction, the melt temperature stops decreasing and further grain nucleation is stifled. Then no new nanoparticles participate in nucleation and the calculation is over. The total number N of grains is all of the nanoparticles participating in the nucleation.[48]

$$N = \sum_{i=1}^{n} N_n \quad [18]$$

The average diameter d of grains can be calculated by:

$$d = \left(\frac{0.5}{N}\right)^{1/3} \quad [19]$$

The calculations were implemented in Matlab. The grain size at different cooling rates was plotted in Fig. 8. The calculation considering blocking factor f by $TiCN_{np}$ is well consistent with the experimental results. Without considering the blocking factor f, the calculated grain sizes are larger than the experimental results. The growth rate of the grain will be faster without the blocking of $TiCN_{np}$. This results in the faster releasing of latent heat and lower undercooling at recalescence.

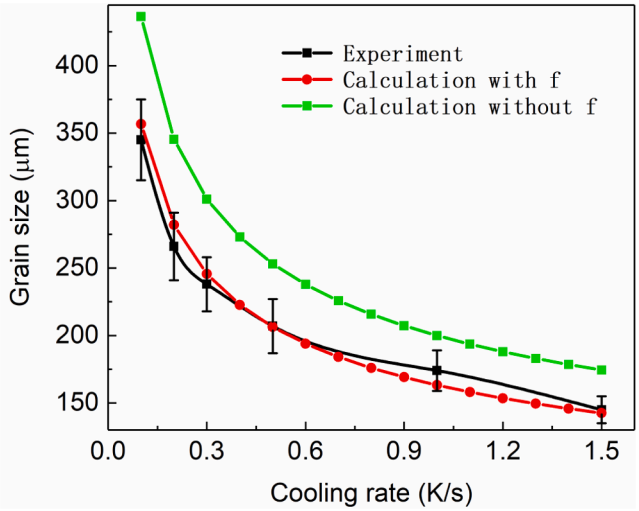

Fig. 8. Grain size of experiments with addition of $TiCN_{np}$ and calculation considering blocking factor f at different cooling rates.

Thus less nucleation has been activated and the grain size will be coarser.

5. Discussion

Engulfment of $TiCN_{np}$ by S/L interface happens above a critical interface velocity that is inversely proportional to particle diameter[49]. The critical velocity would be 1.4×10^{-1} m/s for the $TiCN_{np}$ diameter of 78.2 nm in this work. As shown in our in situ X-radiography results, the S/L interface velocity is $\sim 10 \times 10^{-6}$ m/s, which is four orders of magnitude lower than the critical velocity. This indicates that the $TiCN_{np}$ would be pushed by the interface. As analyzed by Greer[21], Brownian motion of $TiCN_{np}$ is not significant in bring them to the S/L interface in the Al melt. The nanoparticles cannot be spontaneously absorbed by the interface. So we also assume that the nanoparticles are pushed by the growing grain and accumulate at the interface when they meet as shown in Fig. 9. Part of the interface may be coated by nanoparticles, but not the entire interface is wrapped with a layer of nanoparticles. The advancing speed of S/L interface would be retarded by nanoparticles. The coverage ratio ω of $TiCN_{np}$ on the growing grains surface can be calculated by:

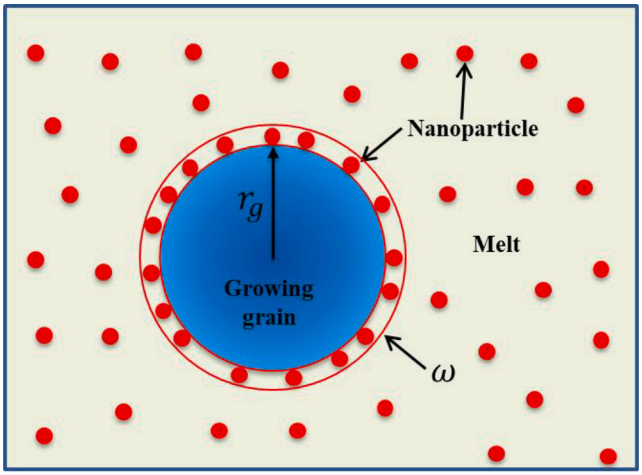

Fig. 9. Schematic of the $TiCN_{np}$ accumulated at the S/L interface.

$$\omega = \frac{\frac{\frac{4}{3}\pi r_g^3 * P_v}{3} * \pi\left(\frac{d}{2}\right)^2}{\frac{4}{3}\pi\left(\frac{d}{2}\right)^3} / 4\pi r_g^2 = \frac{r_g * P_v}{2d} \quad [20]$$

Where r_g is the radius of growing grain, P_v is the volume percent and d is the average diameter of $TiCN_{np}$. As P_v and d are constant at the same addition level of $TiCN_{np}$, the coverage ratio ω is proportional to the critical grain radius. The critical grain radius is the radius when recalescence happened. After recalescence, the melt temperature stops decreasing. There is no new nucleation occurred in the melt and the number density of the grains will not increase.

Taking the weight percent of Ti is 0.26% analyzed by ICP in this study and the density of $TiC_{0.5}N_{0.5}$ to be 4775 kg/m^3, we calculate that the weight percent of $TiC_{0.5}N_{0.5}$ is 0.33 wt% and the volume percent P_v is 0.164 vol%. The average diameter of $TiCN_{np}$ is 78.2 nm in this study. Thus:

$$\omega = \frac{r_g * P_v}{2d} = 1.05\% * r_g(\mu m) \quad [21]$$

At different cooling rates, the critical radius can be calculated from the model as the red line shown in Fig. 10. Then we can determine the coverage ratio of $TiCN_{np}$ at different cooling rates from Eq. [20]. At high cooling rate, there are more grains resulting in smaller critical radius. So the coverage ratio ω of $TiCN_{np}$ decreases with cooling rate. The coverage ratio ω and blocking factor f of $TiCN_{np}$ are well fitted by a linear relationship as shown in Fig. 11(a).

$$f = a + b * \omega \quad [22]$$

Where a and b are constant related to the experimental condition, which are 1.3 and −0.038 in this study. When more nanoparticles accumulate at the S/L interface (larger ω), the blocking effect is better (smaller f). So the blocking effect of $TiCN_{np}$ is linearly increased with the coverage ratio on the surface of the growing grain. As predicted by Greer [21], the growth inhibiting effect of nanoparticles is weakened at higher cooling rates in the same addition level. One reason is that faster migration of S/L interface favors the engulfment of nanoparticles. Another more important reason is that the smaller critical radius at higher solidification rate results in fewer $TiCN_{np}$ accumulating at the S/L interface. The effect of cooling rate and blocking factor f on grain size shows in Fig. 11(b). Generally, the grain size decreases with increasing of cooling rate and decreasing of f . More nanoparticles wrapped on the surface of the growing grains and faster cooling rates will results in finer grain size.

The ultrafine grain structure will exhibit extraordinary properties.

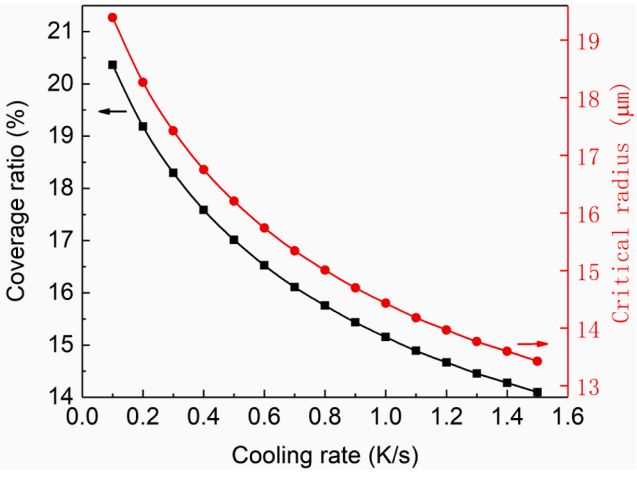

Fig. 10. The critical radius of growing grain and coverage ratio of $TiCN_{np}$ before recalescence at different cooling rates.

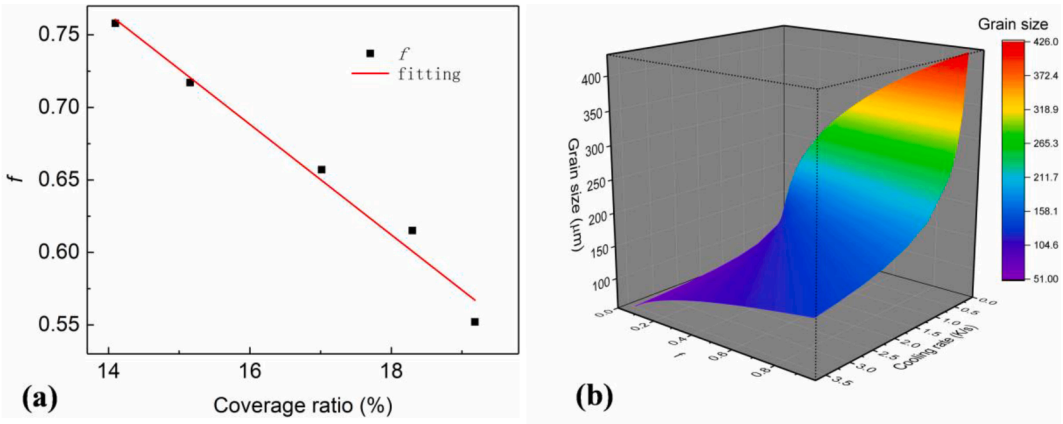

Fig. 11. (a) The relationship between coverage ratio and blocking factor; (b) The effect of cooling rate and blocking factor f on grain size.

With high volume fraction of nanoparticles, the coverage ratio ω is linearly increasing from Eq. 20. The growth restriction effect by nanoparticles would be especially remarkable. Our calculation shows that the grain size can be refined to tens of microns by combining effect of solute and nanoparticles under the slow cooling rate (less than 3.5 K/s). As reported by Cao et al.[50], metal grains size can be refined to nanoscale by high volume percent nanoparticles dispersion in bulk via special method during slow cooling. As shown in Fig. 2, Al-Zr alloy can be obviously refined by $TiCN_{np}$ without poisoning. This is especially beneficial for Aluminum alloys that have poisoning effect inoculated by traditional refiner such as Al-Zr[6], Al-Si[51] and Al-Sc[52].

6. Conclusions

In order to overcome the poisoning effect of Al-Cu-Zr alloy inoculated by Al-5Ti-1B, TiCN nanoparticles were used as grain refiner. In situ X-radiography observation and numerical modeling were adopted to investigate the refinement mechanism of $TiCN_{np}$. The obtained conclusions are as follows:

(1) Al-Zr alloys with addition of Al-Ti-B and $TiCN_{np}$ were studied. The grain size can be effectively refined by $TiCN_{np}$ via ultrasonic treatment as compared with Al-5Ti-1B which has poisoning phenomenon. A small number of $TiCN_{np}$ was dispersed inside the grain and a majority of $TiCN_{np}$ was agglomerated along the grain boundaries.
(2) The effect of Al-Ti-B and $TiCN_{np}$ on Al-Cu-Zr alloy were investigated by in situ synchrotron X-radiography at different cooling rates. The grain size was decreased and the growth rate was increased with the increasing of cooling rate. At the same cooling rate, the grain size with addition of 0.5% $TiCN_{np}$ was smaller than the addition of 0.5% Al-5Ti-1B. The blocking factor f of $TiCN_{np}$ decreases with increasing cooling rate.
(3) A new model considering the growth restriction effect of nanoparticles was established. The growth of grain was restricted by the combining effect of solute and nanoparticles. Nanoparticles accumulated at the S/L interface when they met. The blocking factor f of nanoparticles is linearly decreased with coverage ratio ω which is proportional to the critical grain radius. The grain size decreases with increasing cooling rate and decreasing f.

CRediT authorship contribution statement

Yiwang Jia: Methodology, Resources, Supervision, Validation, Visualization, Writing – original draft, Writing – review & editing. **Dongfu Song:** Data curation, Formal analysis. **Nan Zhou:** Project administration, Resources. **Kaihong Zheng:** Supervision, Validation. **Yanan Fu:** Resources, Software. **Da Shu:** Funding acquisition, Investigation.

Declaration of Competing Interest

The authors declare that they have no known competing financial interests or personal relationships that could have appeared to influence the work reported in this paper.

Acknowledgments

The authors express their gratitude for the financial support from the Project of Science and Technology Development of Guangdong Academy of Sciences (No. 2020GDASYL-20200103140), the Fundamental and Applied Fundamental Research Foundation of Guangdong Province (No. 2020B1515120065) and the National Natural Science Foundation of China (No. U1832183). The experiments were carried out at X-ray Imaging and Biomedical Application Beamline (BL13W1) at Shanghai Synchrotron Radiation Facility (SSRF).

Appendix A. Supplementary data

Supplementary data to this article can be found online at https://doi.org/10.1016/j.ultsonch.2021.105829.

References

[1] X. Zhang, Y. Chen, J. Hu, Recent advances in the development of aerospace materials, Progress in Aerospace Sciences 97 (2018) 22–34.
[2] H. Zhang, N.-P. Jin, J.-H. Chen, Hot deformation behavior of Al-Zn-Mg-Cu-Zr aluminum alloys during compression at elevated temperature, T Nonferr Metal Soc 21 (2011) 437–442.
[3] H. Wu, S.-P. Wen, J.-T. Lu, Z.-P. Mi, X.-L. Zeng, H. Huang, Z.-R. Nie, Microstructural evolution of new type Al–Zn–Mg–Cu alloy with Er and Zr additions during homogenization, T Nonferr Metal Soc 27 (2017) 1476–1482.
[4] W.K. Krajewski, A.L. Greer, J. Buraś, G. Piwowarski, P.K. Krajewski, New developments of high-zinc Al-Zn-Cu-Mn cast alloys, Materials Today: Proceedings 10 (2019) 306–311.
[5] A. Azarniya, A.K. Taheri, K.K. Taheri, Recent advances in ageing of 7xxx series aluminum alloys: A physical metallurgy perspective, J Alloy Compd 781 (2019) 945–983.
[6] Y. Wang, C.M. Fang, L. Zhou, T. Hashimoto, X. Zhou, Q.M. Ramasse, Z. Fan, Mechanism for Zr poisoning of Al-Ti-B based grain refiners, Acta Mater 164 (2019) 428–439.
[7] H. Ding, X. Liu, L. Yu, Influence of zirconium on grain refining efficiency of Al–Ti–C master alloys, J Mater Sci 42 (2007) 9817–9821.
[8] M.A. Easton, M. Qian, A. Prasad, D.H. StJohn, Recent advances in grain refinement of light metals and alloys, Current Opinion in Solid State and Materials Science 20 (2016) 13–24.
[9] D. Qiu, J.A. Taylor, M.-X. Zhang, Understanding the Co-Poisoning Effect of Zr and Ti on the Grain Refinement of Cast Aluminum Alloys, Metall Mater Trans A 41 (13) (2010) 3412–3421.
[10] A.A. Rao, B.S. Murty, M. Chakraborty, Role of zirconium and impurities in grain refinement of aluminium with Al-Ti-B, Mater Sci Tech Ser 13 (1997) 769–777.

[11] Y. Jia, S. Wang, H. Huang, D. Wang, Y. Fu, G. Zhu, A. Dong, D. Du, D. Shu, B. Sun, In Situ Observation of the Zr Poisoning Effect in Al Alloys Inoculated by Al-Ti-B, Metall and Mat Trans A 49 (2018) 4771–4784.
[12] K. Wang, H. Jiang, Q. Wang, B. Ye, W. Ding, A Novel Method to Achieve Grain Refinement in Aluminum, Metall and Mat Trans A 47 (2016) 4788–4794.
[13] K. Wang, G.P. Xu, H.Y. Jiang, Q.D. Wang, W.J. Ding, Effects of TiC0.5N0.5 nanoparticles on the microstructure, mechanical and thermal properties of TiC0.5N0.5/Al-Cu nanocomposites, Journal of Materials Research and Technology 9 (2) (2020) 2044–2053.
[14] K. Wang, H.Y. Jiang, Y.X. Wang, Q.D. Wang, B. Ye, W.J. Ding, Microstructure and mechanical properties of hypoeutectic Al–Si composite reinforced with TiCN nanoparticles, Mater Design 95 (2016) 545–554.
[15] K. Wang, H.Y. Jiang, Y.W. Jia, H. Zhou, Q.D. Wang, B. Ye, W.J. Ding, Nanoparticle-inhibited growth of primary aluminum in Al–10Si alloys, Acta Mater 103 (2016) 252–263.
[16] K. Wang, H.Y. Jiang, Q.D. Wang, W.J. Ding, Influence of nanoparticles on microstructural evolution and mechanical properties of Sr-modified Al-10Si alloys, Materials Science and Engineering: A 666 (2016) 264–268.
[17] L.-Y. Chen, J.-Q. Xu, H. Choi, H. Konishi, S. Jin, X.-C. Li, Rapid control of phase growth by nanoparticles, Nature communications 5 (2014) 3879.
[18] G. Levi, W.D. Kaplan, M. Bamberger, Interfacial phenomena and microstructure evolution during solidification of binary and ternary Al–Mg–Si alloys cast with titanium carbonitride, Materials Science and Engineering: A 326 (2002) 288–296.
[19] K. Wang, G.P. Xu, H.Y. Jiang, Q.D. Wang, B. Ye, W.J. Ding, Development of Al-TiCN nanocomposites via ultrasonic assisted casting route, Ultrasonics Sonochemistry 58 (2019), 104626.
[20] W. Li, J. Mao, J. Feng, Aluminium grain refinement by Ti(C, N) nanoparticles additions: principles, advantages and drawbacks, Metall. Res. Technol. 116 (2) (2019) 212, https://doi.org/10.1051/metal/2018083.
[21] A.L. Greer, Overview: Application of heterogeneous nucleation in grain-refining of metals, The Journal of Chemical Physics 145 (2016), 211704.
[22] D.J. Browne, F. Garcia-Moreno, H. Nguyen-Thi, G. Zimmermann, F. Kargl, R. H. Mathiesen, A. Griesche, O. Minster, Overview of In Situ X-ray Studies of Light Alloy Solidification in Microgravity, JOM: Journal of the Minerals, Metals and Materials Society (2017).
[23] R.H. Mathiesen, L. Arnberg, H. Nguyen-Thi, B. Billia, In Situ X-Ray Video Microscopy as a Tool in Solidification Science, Jom-Us 64 (2012) 76–82.
[24] N.Z. Zongye Ding, Liao Yu, Wenquan Lu, Jianguo Li, Qiaodan Hu, Recent Progress in Metallurgical Bonding Mechanisms at the Liquid/Solid Interface of Dissimilar Metals Investigated via in situ X-ray Imaging Technologies, Acta Metallurgica Sinica (English Letters) 34 (2021) 145–168.
[25] A. Bogno, H. Nguyen-Thi, G. Reinhart, B. Billia, J. Baruchel, Growth and interaction of dendritic equiaxed grains: In situ characterization by synchrotron X-ray radiography, Acta Mater 61 (2013) 1303–1315.
[26] A.G. Murphy, D.J. Browne, Y. Houltz, R.H. Mathiesen, In situ X-ray observations of gas porosity interactions with dendritic microstructures during solidification of Al-based alloys, IOP Conference Series: Materials Science and Engineering 117 (2016), 012067.
[27] W.U. Mirihanage, K.V. Falch, I. Snigireva, A. Snigirev, Y.J. Li, L. Arnberg, R. H. Mathiesen, Retrieval of three-dimensional spatial information from fast in situ two-dimensional synchrotron radiography of solidification microstructure evolution, Acta Mater 81 (2014) 241–247.
[28] Y. Jia, D. Wang, Y. Fu, A. Dong, G. Zhu, D. Shu, B. Sun, In situ Investigation of the Heterogeneous Nucleation Sequence in Al-15 Weight Percent Cu Alloy Inoculated by Al-Ti-B, Metall and Mat Trans A 50 (2019) 1795–1804.
[29] S. Feng, E. Liotti, M.D. Wilson, L. Jowitt, P.S. Grant, In situ mapping of chemical segregation using synchrotron x-ray imaging, MRS Bulletin 45 (2020) 934–942.
[30] Y. Jia, H. Huang, Y. Fu, G. Zhu, D. Shu, B. Sun, D.H. StJohn, An in situ investigation of the solute suppressed nucleation zone in an Al-15 wt% Cu alloy inoculated by Al-Ti-B, Scripta Mater 167 (2019) 6–10.
[31] E. Guo, S. Shuai, D. Kazantsev, S. Karagadde, A.B. Phillion, T. Jing, W. Li, P.D. Lee, The influence of nanoparticles on dendritic grain growth in Mg alloys, Acta Mater 152 (2018) 127–137.
[32] R. Daudin, S. Terzi, P. Lhuissier, J. Tamayo, M. Scheel, N.H. Babu, D.G. Eskin, L. Salvo, Particle-induced morphological modification of Al alloy equiaxed dendrites revealed by sub-second in situ microtomography, Acta Mater 125 (2017) 303–310.
[33] C. Yang, Q. Zhao, Z. Zhang, L. Li, W. Tian, R. Liu, P. Zhang, Y. Xu, Y. Li, Z. Zhang, Q. Jiang, R.O. Ritchie, Nanoparticle additions promote outstanding fracture toughness and fatigue strength in a cast Al–Cu alloy, Mater Design 186 (2020), 108221.
[34] E. Liotti, C. Arteta, A. Zisserman, A. Lui, V. Lempitsky, P.S. Grant, Crystal nucleation in metallic alloys using x-ray radiography and machine learning, Science Advances 4 (4) (2018), https://doi.org/10.1126/sciadv.aar4004.
[35] Y. Jia, S. Wang, D. Shu, Grain size prediction and investigation of 7055 aluminum alloy inoculated by Al–5Ti–1B master alloy, J Alloy Compd 821 (2020), 153504.
[36] Y. Jia, D. Song, N. Zhou, K. Zheng, Y. Fu, D. Shu, In Situ Investigation of Si-Poisoning Effect in Al–Cu–Si Alloys Inoculated by Al–5Ti–1B, Acta Metallurgica Sinica (English Letters) (2021).
[37] Y. Jia, Z. Liu, D. Song, P. Xia, N. Zhou, K. Zheng, Y. Fu, D. Shu, In Situ Investigation of the Solidification of Al-20 wt.% Zn Alloys Inoculated by Al-5Ti-1B, J Mater Eng Perform 30 (2021) 5742–5749.
[38] H. Xie, B. Deng, G. Du, Y. Fu, R. Chen, G. Zhou, Y. Ren, Latest advances of X-ray imaging and biomedical applications beamline at SSRF, nuclear science and techniques 26 (2015) 6–21.
[39] M.X. Zhang, P.M. Kelly, M.A. Easton, J.A. Taylor, Crystallographic study of grain refinement in aluminum alloys using the edge-to-edge matching model, Acta Mater 53 (2005) 1427–1438.
[40] W.T. Kim, B. Cantor, Heterogeneous nucleation of Al2Cu in Al-Cu eutectic liquid droplets embedded in an al matrix, Acta Metallurgica et Materialia 42 (1994) 3045–3053.
[41] A.L. Greer, A.M. Bunn, A. Tronche, P.V. Evans, D.J. Bristow, Modelling of inoculation of metallic melts: Application to grain refinement of aluminium by Al-Ti-B, Acta Mater 48 (2000) 2823–2835.
[42] T.E. Quested, A.T. Dinsdale, A.L. Greer, Thermodynamic modelling of growth-restriction effects in aluminium alloys, Acta Mater 53 (2005) 1323–1334.
[43] Y. Xu, D. Casari, Q. Du, R.H. Mathiesen, L. Arnberg, Y. Li, Heterogeneous nucleation and grain growth of inoculated aluminium alloys: An integrated study by in-situ X-radiography and numerical modelling, Acta Mater (2017) 224–239.
[44] W.W. Mullins, R.F. Sekerka, Morphological Stability of a Particle Growing by Diffusion or Heat Flow, J Appl Phys 34 (1963) 323–329.
[45] I. Maxwell, A. Hellawell, A simple model for grain refinement during solidification, Acta Metallurgica 23 (1975) 229–237.
[46] N.L. Peterson, S.J. Rothman, Impurity Diffusion in Aluminum, Phys Rev B 1 (8) (1970) 3264–3273.
[47] D.a. Shu, B. Sun, J. Mi, P.S. Grant, A quantitative study of solute diffusion field effects on heterogeneous nucleation and the grain size of alloys, Acta Mater 59 (5) (2011) 2135–2144.
[48] A.M. Bunn P.V. Evans D.J. Bristow A.L. Greer J.F. Grandfield D.G. Eskin Essential Readings in Light Metals 2016 Springer International Publishing Cham 387 392 10.1007/978-3-319-48228-6_47.
[49] D. Shangguan, S. Ahuja, D.M. Stefanescu, An analytical model for the interaction between an insoluble particle and an advancing solid/liquid interface, Metallurgical Transactions A 23 (2) (1992) 669–680.
[50] C. Cao, G. Yao, L. Jiang, M. Sokoluk, X. Wang, J. Ciston, A. Javadi, Z. Guan, I. De Rosa, W. Xie, E.J. Lavernia, J.M. Schoenung, X. Li, Bulk ultrafine grained/nanocrystalline metals via slow cooling, Science, Advances 5 (8) (2019), https://doi.org/10.1126/sciadv.aaw2398.
[51] Y. Li, B. Hu, B. Liu, A. Nie, Q. Gu, J. Wang, Q. Li, Insight into Si poisoning on grain refinement of Al-Si/Al-5Ti-B system, Acta Mater 187 (2020) 51–65.
[52] J. Huang, L. Feng, C. Li, C. Huang, J. Li, B. Friedrich, Mechanism of Sc poisoning of Al-5Ti-1B grain refiner, Scripta Mater 180 (2020) 88–92.